



## RESEARCH ARTICLE

# A Method of Computing Accurate 3D Fields of a Quadrupole Mass Filter and Their Use for Prediction of Filter Behavior

John R. Gibson, Kenneth G. Evans, Sarfaraz U. Syed, Simon Maher, Stephen Taylor

Department of Electrical Engineering and Electronics, University of Liverpool, Brownlow Hill, Liverpool L69 3GJ, UK

**Abstract**

A method is described that enables the three-dimensional fields of a simple quadrupole mass filter (QMF) to be determined to a high accuracy. The technique produces accurate field values in the fringe field region as well as in the center of the filter. Using fields obtained typical filter performance is determined and shown to differ from that predicted when fringe fields are ignored. The computed performance shows features obtained experimentally and displays more complex variation with ion mass and other parameters than when fringe fields are ignored.

**Key words:** QMF, Fringe fields, 3-Dimensional

## Introduction

Quadrupole mass filters (QMFs), are widely used analytical tools reviewed by Dawson [1] and by Douglas [2]. Descriptions of QMFs usually use rectangular Cartesian coordinates. A simple filter has four parallel electrodes of constant cross section with their axes parallel to the  $z$ -axis; they are equispaced around the  $z$ -axis and touch the inscribed circle with radius  $r_0$ . Ideal electrodes should have hyperbolic cross sections but, for ease of manufacture, circular cross section electrodes with radius  $r$  are often used, which leads to reduced performance. Computer models of filter behavior assist in determining optimum dimensions for circular electrodes and allow estimates to be made of effects of imperfect manufacture and the non-ideal fields near the filter ends.

For normal filter operation a voltage  $+φ_0$  is applied to one pair of opposing electrodes and  $-φ_0$  to the other pair with

$$\varphi_0 = U - V \cos \omega t \quad (1)$$

To perform a mass scan  $U$  and  $V$  are varied maintaining their ratio constant. Previous results [3–13] modeled filter behavior using electric fields produced by infinitely long

electrodes. Ions are injected in the  $z$  direction and their motions, ion trajectories, are computed over a distance equal to the filter length. Determination of trajectories for many ions starting at different  $x$  and  $y$  positions and different phases of the applied rf field allow filter behavior to be predicted. Such computations show general agreement with many experimental observations but are not usually in exact numeric agreement.

Other computations and investigations [4, 5, 7, 14–22] have attempted to determine the effects on filter behavior arising because electrodes have finite length and because there are end plates, usually at zero potential, to hold the ion source at one end and the detector system at the other. The fields in regions extending from the end plates for some distance into the filter are fringe fields; they are complex and do not match the ideal fields required. Most previous investigations represent the fringe fields using some approximation; early work used a simple linear variation from the ideal field some distance inside the electrodes to zero at the end plates. Later, Hunter and McIntosh [19, 20] determined the fringe fields using a relaxation technique and fitted an exponential expression to these fields.

The fringe field computations reproduce some observed effects; for example, Dawson [15] shows that fringe fields may alter ion trajectories to such an extent that transmission (proportion of ions that pass through the filter at the position of the mass peak) increases compared with the value predicted using fields for infinite length electrodes. The first

Correspondence to: Stephen Taylor; e-mail: s.taylor@liv.ac.uk

investigation of fringe field effects was by Brubaker [14], who used the results to develop rf only pre-filters (delayed DC ramp); pre-filters improve performance and are incorporated in high specification instruments. However, many low-specification instruments, usually known as residual gas analysers (RGAs), do not have pre-filters, and accurate models that predict their behavior for a wide range of conditions are not reported.

As indicated most investigations of fringe fields made approximations; most also used dimensions with  $r/r_0=1.148$  whereas later work [9, 10] showed the optimum value to be in the range 1.125 to 1.130. Further it was found [8] that for infinitely long electrodes, consistent results predicting trends in QMS behavior similar to those observed require very accurate field values. When the results were obtained, only extremely high performance computers had the capability to allow accurate models to be used to investigate filters with finite length electrodes. Advances in computer technology and more elaborate analytical techniques now allow modeling of QMFs with finite length electrodes using desk top computers.

When the electric field used is that for infinitely long electrodes, we refer to the field as a two-dimensional (2D) field because the field in the axial,  $z$ , direction is zero at all positions and the  $x$  and  $y$  field components do not vary in the  $z$ -direction. Fields are computed by solving Laplace's equation with boundary conditions set by the electrodes. We showed [23] that the boundary element method (BEM) formulated as introduced by Read and coworkers [24, 25] produced accurate field values, especially in regions distant from the electrodes where the ions move. This technique was also used by Beaty [26] and by Douglas et al. [27]. Relaxation and other mesh methods tend to be more accurate near electrodes rather than in the region of ion motion; they are also an order of magnitude more demanding in computation resources. A further advantage of this BEM technique is that electric fields can be computed directly from the solution values; relaxation and similar methods produce the potential distribution which must be differentiated to obtain the field values.

Here we describe a technique for accurate field evaluation and use the results to predict the behavior of QMF systems with finite length electrodes and zero potential end plates as shown in Figure 1. For clarity the gaps between the ends of the rods and the end plates are exaggerated in Figure 1.

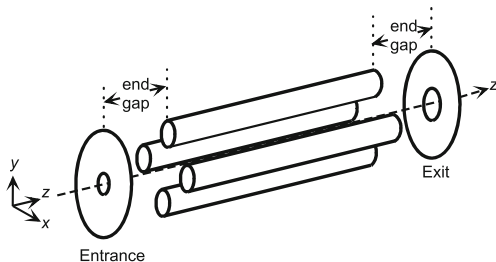


Figure 1. Schematic diagram of a simple QMF

Because all three field components now vary in all directions, we refer to the fields determined as three-dimensional (3D) fields.

## Theory

The method of [23] for 2D fields replaces each electrode by a set of infinite line charges parallel to the filter axis. Points on the electrode surface, referred to as defined points, are required to be at the electrode potential. The potential at each defined point is that due to all the line charges; using this requirement a set of linear equations are developed and solved to determine the line charges. The field components at any required position are determined from the line charges.

For 3D field determination, the electrodes are divided into sections, typically about 100, in the  $z$ -direction. Sections near the electrode ends are very short, 0.05 to 0.1 times  $r_0$ , and section lengths increase towards the center of the filter in a simple geometric progression. Each electrode section is replaced by a set of line charges of the same length and parallel to the  $z$  axis; about 40 line charges per electrode section are adequate. For finite length charges the problem of setting the potential to zero an infinite distance from the charges [23] does not exist so the solution is simplified.

The end plates, at zero potential, are represented using point charges set a short distance inside the plate surfaces facing the QMF electrodes. The number of defined points [23] is double the number of charges and they are placed at the plate surfaces. The fields close to the entrance and exit apertures in the end plates are complicated; the field due to the filter rods, although very weak near the axis, penetrates into the ion source and the field from the ion source electrodes penetrates into the filter region. QMF entrance apertures are usually small and exits large; several models were investigated and are described later.

The relationship between the charge values and the potentials at the defined points in matrix notation is

$$\mathbf{V}_0^T = \mathbf{A}\mathbf{Q}^T \quad (2)$$

where vector  $\mathbf{V}_0^T$  holds values of the desired potentials at the  $M$  defined points, and  $\mathbf{Q}^T$  holds the values of the  $N$  charges.  $\mathbf{A}$  is the  $M$  by  $N$  matrix of the coefficients of the linear equations relating the potentials at the defined points to the charges. Typically  $N$  is 30,000 to 50,000 with  $M$  slightly greater than twice  $N$ .

## Equation Solution

A direct solution of Equation 2 may be written

$$\mathbf{Q}^T = \mathbf{A}^+\mathbf{V}_0^T \quad (3)$$

where  $\mathbf{A}^+$  is the pseudo-inverse of  $\mathbf{A}$  and is found using singular value decomposition, SVD, as previously [23]. The solution yields charge values that give potentials at the

defined points that are closest to the desired values in the least mean squares sense. To reduce computation time the values of  $M$  and  $N$  are halved by setting the entrance and exit hole diameters equal and using the symmetry about the center of the filter. Two solutions are obtained, one for each diameter, and the result is formed by changing from one solution to the other at the filter mid point where the field is 2D.

Unfortunately for accurate modeling, the matrix  $\mathbf{A}$  is so large that calculation of its pseudo-inverse is unacceptably long; it requires several days with a high performance desk top computer. The following iterative solution reduces the time to an acceptable one using a multi-threaded approach with a four-core AMD Phenom II or Intel Core I7 and 16GBytes of RAM.

Equation 2 is partitioned by choosing half the number of rod sections,  $H$ , such that it is divisible by an integer,  $D$ , in the range 4 to 16 with 4 or 8 most often selected. If the number of line charges on a group of  $D$  sections is  $A$  then the number of charges on the end plates is chosen to be an integer  $B$  multiplied by  $A$ ;  $B$  is usually between 3 and 8. The system is divided into  $S = \frac{H}{D} + B$  sets of equal numbers of charges. For clarity the method is illustrated with  $S=4$  although in practice  $S$  is usually between 8 and 16. The equations are partitioned and approximated by  $S$  separate equations as illustrated by the blocks in Figure 2. Each equation is solved separately using the SVD method which decomposes the matrix into the SVD components from which the charges are determined. Because the time taken by the SVD algorithm, although variable, is approximately the cube of the number of unknowns being determined the total time to solve all  $S$  equations reduces to, at most, a few hours depending on the number and size of partitions.

The partitioned form of Equation 2 may be written as

$$\begin{bmatrix} \mathbf{V}_1^T \\ \vdots \\ \mathbf{V}_S^T \end{bmatrix} = \begin{bmatrix} \mathbf{A}_{11} & \cdots & \mathbf{A}_{1S} \\ \vdots & \ddots & \vdots \\ \mathbf{A}_{S1} & \cdots & \mathbf{A}_{SS} \end{bmatrix} \begin{bmatrix} \mathbf{Q}_1^T \\ \vdots \\ \mathbf{Q}_S^T \end{bmatrix} \quad (4)$$

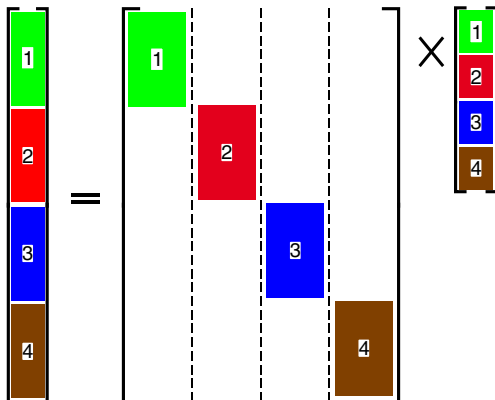


Figure 2. Partitioning of the matrix equation

where partition  $\mathbf{V}_i$  contains the voltages for the defined points closest to charges of the partition  $\mathbf{Q}_i$ . One row of Equation 4 may be written

$$\mathbf{V}_i^T = \sum_{j=1}^S \mathbf{A}_{ij} \mathbf{Q}_j^T = \mathbf{A}_{ii} \mathbf{Q}_i^T + \sum_{j \neq i} \mathbf{A}_{ij} \mathbf{Q}_j^T \quad (5)$$

The potential at any position on an electrode or end plate is most strongly affected by the charge elements closest to that position. Hence, to a first approximation, the solution is obtained by solving  $S$  equations

$$\mathbf{V}_i^T \approx \mathbf{A}_{ii} \mathbf{Q}_i^T \quad (6)$$

Independent solutions of each of the  $S$  equations, with the form of Equation 6, produces first approximations  $\mathbf{Q}_{i,1}$  for the charges. Generalizing Equation 5 gives an iterative formula, Equation 7, for improving the solutions.

$$\mathbf{A}_{ii} \mathbf{Q}_{i,(n+1)}^T = \mathbf{V}_i^T - \sum_{j \neq i} \mathbf{A}_{ij} \mathbf{Q}_{j,n}^T \quad (7)$$

All the matrices  $\mathbf{A}_{ij}$  and the pseudo-inverse matrices  $\mathbf{A}_{ii}^+$  are calculated once only and the values stored in main memory for rapid execution of the iterations. One iteration takes approximately 1 s with a current generation desktop computer using the precalculated matrices; most of the calculation time is taken in evaluating the  $\mathbf{A}_{ij}$  and  $\mathbf{A}_{ii}^+$  matrices.

The choice of the value of  $S$  controls the time to calculate the matrices; a large value of  $S$  results in small matrices  $\mathbf{A}_{ij}$  and rapid calculation of the pseudo-inverse matrices  $\mathbf{A}_{ii}^+$ . However, as  $S$  increases the approximation in Equation 6 becomes poorer and instability can result in the iteration process.  $S$  must be small enough to ensure convergence while, at the same time, large enough to make the calculation time acceptable. Using  $N$ ,  $M$ , and  $S$  with the suggested ranges, the process rarely fails to converge. If divergence occurs, it is rapid and charge values outside the computer's allowed numeric range are produced, providing a simple detection method. In the few unstable cases found, adjustment of partitioning and the numbers of charges enabled a converging solution to be found. Convergence usually takes from 500 to 2000 iterations, although for some models of the end plate up to 5000 iterations may be required. The total time of matrix calculation and iteration is between 1 and 8 h, which is acceptable as this is only required once to study behavior of any proposed design of RGA.

### Field Determination

To compute an ion trajectory, the field is required at every position of the ion as it is tracked using a Runge–Kutta

algorithm. Exact field evaluation at each point, while computing the trajectory, is too slow. Instead, the three field components are determined at all points on a set of uniform square grids, and interpolation used to find the field at any point. The grids have sides  $2 \times r_0$  and are in planes at right angles to the filter axis; that is,  $z$  is constant over each grid plane. The planes are not equally spaced; spacing is very small in the regions near the end plates, typically  $0.002r_0$  to  $0.01r_0$ , as the field changes rapidly in the  $z$  direction and is larger, about  $1.5r_0$  to  $2.0r_0$ , near the center of the filter. Around 800 sets of grid values are used for a typical RGA with length in the range  $25r_0$  to  $50r_0$ .

For each  $z$  position, all components of the field are determined at all grid points using the charges obtained from the solution of the matrix equation. To determine filter behavior using 2D fields, it was found [8] that a grid interval of  $0.002 \times r_0$ , or less, was necessary for accurate results using bi-linear interpolation to determine the field at an ion's actual position. Usually grids of 1601 by 1601 points (1600 intervals) were used requiring approximately 40MBytes of memory to hold one grid. When linear interpolation is extended to three dimensions this is tri-linear interpolation. However, the use of 3D grids of the size used for 2D interpolation at 800  $z$  positions with three field components would require 48GBytes of memory. When the work started this exceeded the amount that could be fitted to a desk top computer and the grid value computation time would be over a week even on the computer eventually used.

Instead of linear interpolation a complete three dimensional second order interpolation process was developed; this was constrained by adding a requirement that the results satisfied Maxwell's Equations. The process results in a set of 15 coefficients associated with a cuboid defined by eight lattice nodes; the coefficients are only evaluated once at every grid position and stored for use computing ion trajectories when determining filter performance.

Interpolation methods were tested with known field distributions similar to those found in the fringe field regions at the end of the electrodes as this is where changes in all field components are greatest and interpolation accuracy will be lowest. The magnitudes of  $x$  and  $y$  were less than  $0.8 \times r_0$  to avoid the fluctuations that occur in computed fields close to the electrodes. Over  $10^5$  points were selected distributed throughout this region and an error computed by summing the squares of the differences between the field magnitude and the interpolated value. The RMS error is the square root of this sum divided by the number of interpolation points. Figure 3 illustrates test results and shows that the RMS errors for a grid with 1600 intervals using the chosen field region are less than  $10^{-7}$  using tri-linear interpolation. The results for the second order interpolation method show that it achieves the same accuracy with a grid interval ten times larger.

In practice, grids of about 250 intervals were used; even allowing for the extra storage required for the coefficients, the complete set of grids required just over 6 GB of memory. The time to compute all the grid points fell to a few hours

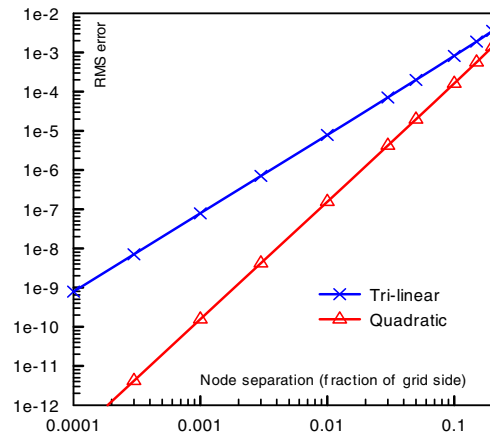


Figure 3. Interpolation errors as a function of grid interval

and the effect of the more complicated interpolation on the computation time of ion trajectories was acceptable.

### Determining QMF Behavior

Once the 3D fields are known QMF behavior is determined as for 2D fields [23] except that the  $z$  component of the field is finite; it is significant near the end plates and all three field components vary in all three directions. For 2D fields the  $z$  component of the field is zero everywhere so the  $z$  component ion velocity is constant; also the  $x$  and  $y$  field components do not vary in the  $z$  direction. Ions originate with random rf phase at random positions on a circular disc with  $z$  coordinate that of the end plate surface facing the electrodes. A fourth order Runge–Kutta algorithm is used to trace the motions of large numbers of ions through the filter. This is the 2D field program modified to include the non-zero  $z$  component of the field and variation of all field components in the  $z$  direction. The ion motion is more complicated for the 3D system so slightly smaller time steps were used when evaluating the Runge–Kutta algorithm although tests indicated that this was not essential.

Unlike the 2D case, different field calculations are required for each length of filter; separate calculations are also necessary for each different gap between the end plates and the electrodes and for different entrance and exit apertures. However, all dimensions and voltages may be scaled linearly without affecting the field geometry; fields were evaluated with filters described using lengths in units such that  $r_0=1$  and, for normal operation, unit voltages on the electrodes. The behavior of a particular filter only requires the grids of field interpolation coefficients, the actual dimension  $r_0$ , the position on the mass scale, the frequency of the applied rf, and the resolution setting in order to determine the path any ion takes through the filter.

### Model Testing

While the model was tested in many ways a useful requirement to be met by any model of ion motion in a

time varying electric field results from the following analysis. At any point in a 3D field a charge particle moves according to Newton’s Second Law, such that

$$m \frac{d^2 \mathbf{s}}{dt^2} = Q\mathbf{E} \quad (8)$$

where  $m$  is the ion mass,  $Q$  its charge,  $\mathbf{s}$  is the vector from the origin to the current position and  $\mathbf{E}$  is the electric field; both  $\mathbf{s}$  and  $\mathbf{E}$  have components in all three directions and vary with time.

Normalize spatial dimensions using  $\xi = \frac{s}{r_0}$  and normalize time using  $\tau = \omega t$  where  $\omega$  is the angular frequency of the applied rf. Replacing  $\mathbf{E}$  using  $\mathbf{E} = \frac{V\boldsymbol{\varepsilon}}{r_0}$  where  $\boldsymbol{\varepsilon}$  is a function of the normalized field, time and resolution setting. The equation of motion may be written

$$m \frac{d^2 \xi}{d\tau^2} = \lambda \boldsymbol{\varepsilon} \quad (9)$$

where

$$\lambda = \frac{QV}{m\omega^2 r_0^2} \quad (10)$$

If Equation 9 is used to find the trajectory of an ion within a filter for various combinations of the parameters  $m$ ,  $V$  and  $\omega$ , then each solution will be the same provided that the value of  $\lambda$  is the same and, in addition, the initial conditions (initial normalized spatial position, normalized velocity of the ion and the phase of the rf field) are the same.

The filter behavior is obtained by finding the trajectories of ensembles of ions; each ensemble typically has  $10^5$  to  $10^6$  ions with a large randomized spread of starting conditions. A different ensemble is used at each of a number of settings of electrode voltages  $U$  and  $V$  (with constant value of the resolution setting  $\frac{U}{V}$ ) corresponding to different positions on the mass scale. The percentage of ions transmitted at each position is recorded and used to produce a simulated mass peak. If identical ensembles of ions (identical normalized starting conditions) are used then identical results should be obtained if  $\lambda$  and the resolution setting are the same. That is, many different combinations of ion mass, initial ion energy and rf frequency should produce identical results. This test was applied to a large number of results and showed that filter behavior using fields and trajectories, computed as described, satisfied this requirement.

## Results

### Computations

Because of the large computing effort necessary to determine filter behavior for variation of all parameters most initial investigations were restricted to circular section electrodes with  $r/r_0=1.127$ . A number of models of the apertures in the entrance end plate were tested ranging from

ignoring the aperture to a shallow, about  $0.5r_0$  deep, recess using various aperture diameters up to  $0.5r_0$ . Hunter and McIntosh [19] state that the effect of an aperture on the fringing fields is negligible for aperture radius less than  $0.5r_0$ . We did find small changes in fringe fields with aperture size, which produced small, but insignificant, variations in QMF behavior and have used the model with a recess for the results presented. The choice of model used to represent the exit end plate has little effect on QMF performance and is discussed later.

Results shown are for a typical RGA with  $r_0=2.76$  mm, rod length 100 mm, both end gaps 1 mm and a source radius of 1 mm. Most computations used an rf frequency of 4 MHz although tests were performed to confirm that frequency changes, with changes in mass and energy made to maintain  $\lambda$  constant, produced identical results. Typical results at moderate ion energies are shown in Figure 4 for several settings of filter resolution with 4 eV mass 4 ions. We define the filter resolution setting by  $\eta$  where

$$U = \eta kV \quad (11)$$

$U$  is the applied DC voltage,  $V$  is the amplitude of the applied rf voltage and  $k \approx 2.979$  corresponds to the peak of the lower stability zone; hence  $\eta=1$  corresponds to the

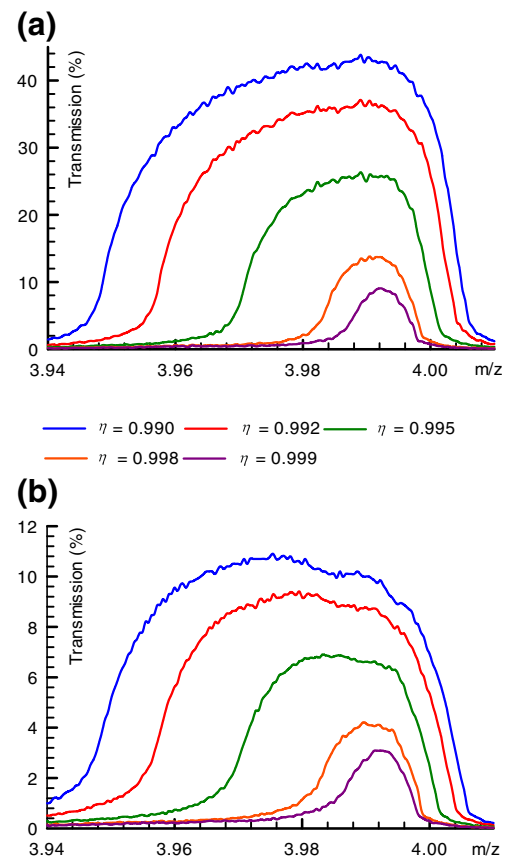


Figure 4. Predicted QMF mass scan peaks using (a) 3D fields, (b) 2D fields

limiting value of resolution for an ideal filter with hyperbolic electrodes. Results in Figure 4 are for low mass, hence high velocity, ions where the effect of the fringe fields on the 3D results is not so large that the mass peaks are grossly distorted. Under these conditions, the peaks using 2D and 3D fields are similar in shape although the maximum transmissions (height of the mass peak) differ significantly; transmission is computed as the percentage of the injected ions that pass through the filter and reach the detector.

Conditions selected for Figure 4 are such that fringe field effects are not large; for a wider range of conditions, results using 2D and 3D fields often produce different peak shapes. Using 3D fields there is usually a much smaller low mass tail and the range of peak shapes is larger with some peaks extremely distorted compared with those for an ideal filter. Maximum transmission differs using 2D and 3D fields with both significantly larger and smaller transmissions being found using 3D fields.

In general, there is much greater variation in performance determined for a particular filter design using 3D fields than using 2D ones. Changing the separations between the rods and end plates, or changing the manner in which the entrance aperture is modeled, both predict large changes in behavior. A few peak shapes are illustrated later and compared with experimental results.

Using 2D fields and circular section electrodes, provided ions experience at least seventy cycles of the rf field, the peak height is almost constant for fixed QMF dimensions, resolution setting and frequency [8]. If ions experience more than 70 rf cycles, transmission decreases very slightly. For results using the 3D fields the transmission behaves in a much more complicated manner; this is illustrated by examining the heights of mass peaks for simulated mass scans using one filter geometry and a range of ion masses and energies. Because behavior is the same for a fixed value of  $\lambda$ , Equation 10, the results are shown as mass peak height as a function of initial ion velocity which is proportional to  $(V_{ion}/m)^{\frac{1}{2}}$  where  $V_{ion}$  is the nominal ion source accelerating voltage. Figure 5 shows the results with the filter dimensions used for Figure 4; several different ion masses are required to cover the ion velocity range shown when ion energy is

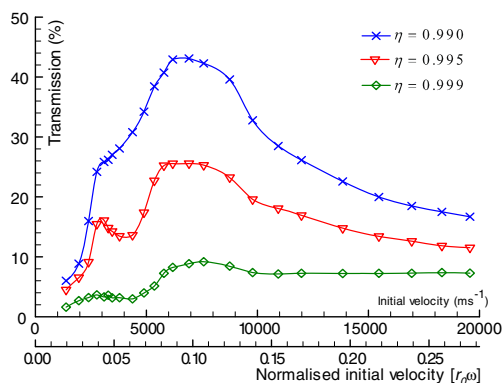


Figure 5. Mass peak height variation with ion velocity

restricted to typical values used in practice. If any filter dimension is changed, the curves change by a large amount. There is always a peak but both its height and position vary. There is usually a complex structure on the low velocity side of the peak and a smoothly changing form on the high velocity side.

The second, normalized velocity, abscissa in Figure 5, is to illustrate that many combinations of filter parameters lead to the same value of transmission. Using the normalized velocity scale the peak transmission is at approximately  $0.1 \times r_0 \text{ rad}^{-1}$ , which is equivalent to approximately 1.6 cycles per  $r_0$ . A similar value of ion velocity for peak transmission was found by Dawson [16].

Ehlert [28] shows experimental results with features found in Figure 5, and computations by Dawson [5, 16] show similar trends. In [5, 16, 28], the horizontal axis is in the opposite sense to that of Figure 5; it is drawn as a function of ion mass with all ions having the same energy. Consequently, for [5, 16, 28] the axis scale is proportional to the inverse of the ion velocity squared. Ehlert's curve does show a small amount of structure corresponding to that to the left of the peak in Figure 5, but it is not as great; however we found that small changes in end gaps, source radius, frequency, and resolution setting produce very large changes in the curves.

An investigation was made to determine the distance into the filter after which the fringe fields may be ignored and behavior can be modeled using 2D fields. The field was modified so that it changed from the 3D to the 2D field at different distances into the filter; very small effects were observed when the change was at distances from about  $7.5 \times r_0$  down to  $2.5 \times r_0$ , but significant effects on filter behavior were observed with the changes at distances of  $2.5 \times r_0$  or less.

The effect of the fringe field at the exit end plate was found to be negligible; even an extreme case using the 2D fields from the center of the filter to the exit position produced only small changes in the results. Provided the filter is longer than about  $25 \times r_0$ , very few ions that reach the exit fringe field region ever move a distance greater than  $r_0$  from the axis, regardless of the model used to create the fringe field. For all forms of exit aperture model examined, all the ions that reached the exit position with their distance from the axis less than  $r_0$  were regarded as transmitted. Examining behavior when only ions inside a smaller radius at the exit position are considered to be transmitted produced complex effects, including peak splitting, and are observed experimentally [21, 22].

### Experimental Results

Measurements were made with an MKS Microvision Plus RGA, which has dimensions close to those of the typical system used for the previous figures. It was only possible to obtain measurements providing short sections of curves similar those of Figure 5 because the range of ion velocities

shown requires measurements for ions with several different masses and energies. The output of any ion source varies with mass and nominal energy of ejection of the ions from the source and the variation is usually unknown. Hence, the actual filter transmission value cannot be determined experimentally although variation in transmission can be measured over a small range of ion velocity. There are few quantitative studies of ion source behavior; those there are, for example [29], show that behavior is complicated and output may vary with ion mass, ion energy, ion type and even with time.

Although curves showing variation of filter transmission with initial ion velocity could not be determined experimentally for a wide range of conditions it was possible to obtain results showing the variation in mass peak shape with ion mass. Figure 6 compares mass peaks for four ion species using the MKS instrument and computed ones using the dimensions and operating frequency of the RGA. The mass scale for the measurements has been adjusted to align measurements and the computations as the two mass scales are calibrated using different methods. The experimental signal is scaled to match the transmission predicted by the model because the input ion current is unknown. A further feature of commercial instruments, such as the MKS Microvision Plus, is that resolution is automatically adjusted with position on the mass scan so that peak width,  $\Delta m$ , is constant. The model follows the usual theoretical description

of QMF devices (a fixed scan line passing through the origin of the stability diagram) and maintains resolution,  $\Delta m/m$ , constant. The resolution was adjusted for each computation of a mass peak so that the peak width approximately matched the measured one; for mass four ions, the resolution is extremely low. For best fit to the experimental data the ion energy used for the computed peaks was slightly lower than that indicated by the instrument.

To produce Figure 6, a fixed end gap and ion source model were used with the ion energy set at 3 eV; the MKS Microvision Plus ion energy was set to a nominal value of 4 eV. It is possible to obtain better agreement for each ion mass if the end gap value, ion source model, and experimental setting of ion energy are varied by small amounts with mass. The ion source model is simpler than an actual ion source having uniform illumination, no energy spread and no beam spread. The ion source and ion extraction of the MKS instrument will produce a more complicated ion beam which will probably vary with ion mass.

The mass peaks in Figure 6, although not identical, show similar trends in peak shape variation for the computations and experiment. Mass peaks obtained computed for an ideal QMF (hyperbolic electrodes and no fringe fields) show a rather rounded shape, similar to those in Figure 4, and this is also true of many observations using QMFs. However, the model and the experiment both produce distorted peaks with

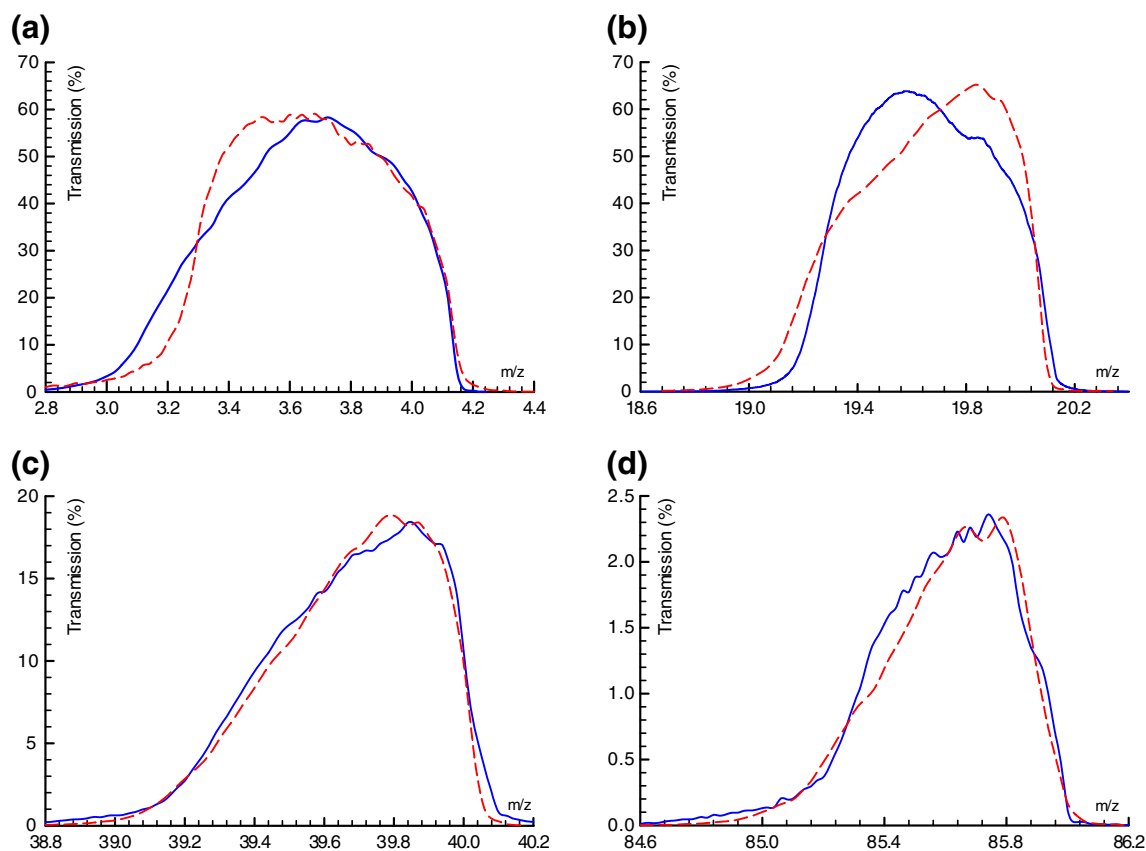


Figure 6. Comparison of computed (solid blue line) and measured (broken red line) mass peaks

the most severe distortion at the higher masses (lower ion velocity) in Figure 6. At the higher masses, the peaks have a ‘triangular’ shape and the shapes change towards the more usual form as the ion mass is decreased although the model shows a more rapid change in shape than the experiment. The model is able to produce results at even lower ion velocities than is possible experimentally and the peaks become even more distorted.

Titov [7] suggests that fringe fields may lead to the formation of precursors. We have seen no evidence of this in the results obtained using the model; we only see them with a displaced electrode or an incorrect voltage on one electrode. With very large end gaps, the computed mass peaks do exhibit structure; this might appear to be precursor formation.

## Discussion and Conclusions

The results of Figure 5 confirm and expand those of Dawson [5, 16] and Ehlert [28]; the filter behavior shown by Figure 5 and [5, 16, 28] can be divided into two regions. If conditions are such that the operation of the filter corresponds to the region from the peak position of the curves to higher ion velocities, the behavior is similar to that predicted by the 2D model except that peak heights are usually larger; in some cases, by nearly an order of magnitude. Peak height falls towards the value for 2D fields as ion velocity increases although convergence is very slow. In this high ion velocity region peak shapes are generally similar to those for 2D fields and resolution (peak width) is almost the same for the 2D and 3D fields. The reduction in the low mass tail found with 3D fields means that where mass peaks with large height differences are close together results using 3D fields suggest that the peaks will be more easily resolved than is predicted using 2D fields.

For the region of Figure 5 with ion velocities below the peak position, the variation of transmission is more complicated and varies with changes in filter geometry. Mass peak shape and height vary by a large amount for small changes in initial ion velocity, and peaks often have distorted shapes. In some cases, the distorted shapes result in improved resolution but as peak shape varies rapidly with ion velocity (with mass if ion energy is constant) the resolution varies with mass. The results obtained so far give no obvious general rules governing behavior in this low ion velocity region. The mass peak distortion depends strongly on how the source region is modeled; distortion does appear to increase slightly when the diameter of the ion source is decreased.

Different filter behavior in the two regions arises because of the different number of cycles of the rf field ions experience while in the fringe field region. At velocities higher than the value at the peak position of Figure 5, ions experience less than one rf cycle while in the fringe field. Conversely, ions entering the filter with low initial velocity experience many rf cycles while in the fringe field; some ions are lost while in the fringe field and the remainder enter

the region beyond the fringe field with positions and velocities that do not lead to trajectories such that the ions pass through the filter.

The very variable results for transmission and large variation in mass peak shape obtained for low ion velocity values suggest that a QMF should be operated such that the highest mass ion to be observed has a velocity slightly higher than the position of the peak of Figure 5. Filters are normally operated with fixed ion energy so the filter sensitivity (transmission) will be higher for high mass ions than for low ones. For a given choice of QMF length and end gap, the peak position in Figure 5 is set by the combination of ion energy (ion velocity) and operating frequency. The highest mass ions should experience less than one rf cycle while in the fringe field. Once ion energy and operating frequency are set, the number of cycles experienced by an ion passing through a filter can be determined for any ion mass; as mass falls, the number of cycles falls, and filter performance decreases. Hence, the model is suggesting that mass range of a particular design of RGA is restricted by the fringe fields at the entrance. Choice of a high upper mass will raise the useful low mass limit.

The techniques described allow accurate computation of the fields within a full 3D model of a QMF device; so far they have only been applied to systems without a pre-filter or a post-filter. Results obtained show very complicated behavior, especially if ion velocities are low, and suggest that ion velocity should be above some limiting value that the computations using the techniques described can determine. The value must be determined for each design of QMF; even small modifications in dimensions may produce large changes in predicted performance.

Imperfections of construction or applied voltages in a QMF were examined for 2D fields [13]. For 3D systems, a much larger range of imperfections are possible, we have only examined cases similar to those in [13] and obtained similar results.

## References

1. Dawson, P.H.: *Quadrupole Mass Spectrometry and Its Applications*. Elsevier, Amsterdam (1976)
2. Douglas, D.J.: Linear quadrupoles in mass spectrometry. *Mass Spectrom. Rev.* **28**, 937–960 (2009)
3. Dawson, P.H., Whetten, N.R.: Non-linear resonances in quadrupole mass spectrometers due to imperfect fields. II. The quadrupole mass filter and monopole mass spectrometer. *Int. J. Mass Spectrom.* **3**, 1–12 (1969)
4. Dawson, P.H.A.: detailed study of the quadrupole mass filter. *Int. J. Mass Spectrom.* **14**, 317–337 (1974)
5. Dawson, P.H.: Ion optical properties of quadrupole mass filters. *Adv. Electron Phys.* **53**, 153–208 (1980)
6. Titov, V.V.: Ion separation in imperfect fields of the quadrupole mass analyzer Part I. Ion beam dynamics in the phase-space. *Int. J. Mass Spectrom. Ion Process.* **141**, 13–26 (1995)
7. Titov, V.V.: Ion separation in imperfect fields of the quadrupole mass analyzer Part V. Experimental verification. *Int. J. Mass Spectrom. Ion Process.* **141**, 57–65 (1995)
8. Gibson, J.R., Taylor, S.: Prediction of quadrupole mass filter performance for hyperbolic and circular cross section electrodes. *Rapid Commun. Mass Spectrom.* **14**, 1669–1673 (2000)

9. Gibson, J.R., Taylor, S.: Numerical investigation of the effect of electrode size on the behavior of quadrupole mass filters. *Rapid Commun. Mass Spectrom.* **15**, 1960–1964 (2001)
10. Douglas, D.J., Kononkov, N.V.: Influence of the 6th and 10th spatial harmonics on the peak shape of a quadrupole mass filter with round rods. *Rapid Commun. Mass Spectrom.* **16**, 1425–1431 (2002)
11. Gibson, J.R., Taylor, S.: Asymmetrical features of mass spectral peaks produced by quadrupole mass filters. *Rapid Commun. Mass Spectrom.* **17**, 1051–1055 (2003)
12. Kononkov, N.V., Londry, F., Ding, C., Douglas, D.J.: Linear quadrupoles with added hexapole fields. *J. Am. Soc. Mass Spectrom.* **17**, 1063–1073 (2006)
13. Taylor, S., Gibson, J.R.: Prediction of the effects of imperfect construction of a QMS filter. *J. Mass Spectrom.* **43**, 609–616 (2008)
14. Brubaker, W.M.: An improved quadrupole mass analyzer. *Adv. Mass Spectrom.* **4**, 293–299 (1968)
15. Dawson, P.H.: Fringing fields in the quadrupole mass filter. *Int. J. Mass Spectrom. Ion Phys.* **6**, 33–44 (1971)
16. Dawson, P.H.: The acceptance of the quadrupole mass filter. *Int. J. Mass Spectrom. Ion Phys.* **17**, 423–445 (1975)
17. Dawson, P.H.: Fringing fields in quadrupole-type mass analyzers. *J. Vac. Sci. Technol.* **9**, 487–491 (1972)
18. Titov, V.V.: Ion separation in imperfect fields of the quadrupole mass analyzer Part II. Ion beam dynamics in the phase-space of the fringing field. *Int. J. Mass Spectrom. Ion Process.* **141**, 27–35 (1995)
19. Hunter, K.L., McIntosh, B.J.: An improved model of the fringing fields of a quadrupole mass filter. *Int. J. Mass Spectrom. Ion Process.* **87**, 157–164 (1989)
20. McIntosh, B.J., Hunter, K.L.: Influence of realistic fringing fields on the acceptance of a quadrupole mass filter. *Int. J. Mass Spectrom. Ion Process.* **87**, 165–179 (1989)
21. Blaum, K., Geppert, Ch, Muller, P., Nortershauser, W., Otten, E.W., Schmitt, A., Trautmann, N., Wendt, K., Bushaw, B.A.: Properties and performance of a quadrupole mass filter used for resonance ionisation mass spectrometry. *Int. J. Mass Spectrom.* **181**, 67–87 (1998)
22. Blaum, K., Geppert, Ch, Muller, P., Nortershauser, W., Wendt, K., Bushaw, B.A.: Peak shape for a quadrupole mass spectrometer: comparison of computer simulation and experiment. *Int. J. Mass Spectrom.* **202**, 81–89 (2000)
23. Gibson, J.R., Evans, K.G., Taylor, S.: Modeling mass analyzer performance with fields determined using the boundary element method. *J. Mass Spectrom.* **45**, 364–371 (2010)
24. Read, F.H.: ‘Zero gap’ electrostatic aperture lenses. *J. Phys. E* **4**, 562–566 (1971)
25. Read, F.H., Adams, A., Soto-Montiel, J.R.: Electrostatic cylinder lenses. I. Two element lenses. *J. Phys. E* **4**, 625–632 (1971)
26. Beaty, E.C.: Calculated electrostatic properties of ion traps. *Phys. Rev. A* **33**, 3645 (1986)
27. Douglas, D.J., Glebova, T.A., Kononkov, N.V., Sudakov, M.Y.: Spatial harmonics of the field in a quadrupole mass spectrometer with circular electrodes. *Tech. Phys.* **44**, 1215–1219 (1999)
28. Ehlert, T.C.: Determination of transmission characteristics in mass filters. *J. Phys. E* **3**, 237–239 (1970)
29. Austin, W.E., Leck, J.H., Batey, J.H.: Study of the performance of a group of quadrupole mass spectrometers. *J. Vac. Sci. Technol., A* **10**, 3563–3567 (1992)